International Journal of Cast Metals Research

ISSN: 1364-0461 (Print) 1743-1336 (Online) Journal homepage: http://www.tandfonline.com/loi/ycmr20

# Effect of sand dilation on distortions and pattern allowances during steel sand casting

D. Galles & C. Beckermann

**To cite this article:** D. Galles & C. Beckermann (2017) Effect of sand dilation on distortions and pattern allowances during steel sand casting, International Journal of Cast Metals Research, 30:5, 257-275, DOI: 10.1080/13640461.2017.1290909

**To link to this article:** http://dx.doi.org/10.1080/13640461.2017.1290909

Published online: 15 Feb 2017.

INTERNATIONAL JOURNAL OF CAST METALS RESEARCH, 2017
VOL. 30, NO. 5, 257–275
https://doi.org/10.1080/13640461.2017.1290909

Taylor & Francis
Taylor & Francis Group



# Effect of sand dilation on distortions and pattern allowances during steel sand casting

D. Galles and C. Beckermann

Department of Mechanical and Industrial Engineering, University of Iowa, Iowa City, IA, USA

**ARTICLE HISTORY**
Received 1 September 2016
Accepted 28 January 2017

**KEYWORDS**
Steel casting; pattern allowances; distortions; stress analysis; sand dilation

**ABSTRACT**
Mechanical interactions between the sand mold and casting have a great impact on pattern allowances. In this study, the effect of core expansion on distortions during steel casting is investigated. A hollow steel cylinder is cast using silica and zircon sand cores. The evolution of the cylinder's inner diameter is measured *in situ* using LVDTs. During solidification, core expansion is found to distort the inner diameter into a barrel-shaped profile, generating the largest expansion at the mid-height. The experiments are simulated using a sequential thermo-mechanical coupling. In the stress analysis, the steel and sand are modeled using an elasto-visco-plastic constitutive law and the Drucker–Prager Cap model, respectively. The simulations reveal that sand dilation due to shear stresses, as opposed to thermal expansion, accounts for the majority of the increase in the inner diameter. The measured and predicted pattern allowances are found to be in excellent agreement.



## 1. Introduction

During sand casting, mechanical interactions between the casting and mold generate distortions, which in turn influence pattern allowances (*PA*):

$$PA[\%] = \frac{feature\ length_{initial} - feature\ length_{final}}{feature\ length_{initial}} \times 100 \quad (1)$$

In Equation (1), *feature length* is the dimension for any particular feature. The *initial* and *final* subscripts denote that the measurements are taken from the pattern and casting, respectively. In the absence of distortions, pattern allowances are attributed solely to thermal strains and commonly referred to as the patternmaker's shrink (e.g. the patternmaker's shrink is approximately 2.1% for steel). From this viewpoint, distortions can be defined as deviations from the patternmaker's shrink.

Distortions can create dimensional inaccuracies in the as-cast part that are difficult to remedy. Often, patterns are designed using a time-consuming trial-and-error method in which several design iterations are needed to achieve the desired dimensions. Also, distortions are sensitive to process conditions (e.g. packing density of the mold and cores), causing variations in pattern allowances that may require post-casting operations such as straightening, welding or machining. Furthermore, distortions occurring near the end of solidification may generate cracks, necessitating the casting to be scrapped. Therefore, mitigation of these problems will result in high quality castings and lead to efficient casting processes.

Distortions are created by several physical phenomena, including uneven cooling, mold (or core) restraint, and mold (or core) expansion. Uneven cooling occurs in castings with variable section thicknesses. The thinner sections of a casting cool (and thus contract) faster than thicker sections, generating stresses and associated distortions. Mold restraint constrains thermal contractions in the casting and generates distortions at times ranging from the end of solidification until shakeout. Defects caused by mold restraint are a well-established problem and have been the focus of previous experimental studies [1–6]. The studies usually involved casting a slender bar with flanges on both ends to induce mold restraint [1–5]. The experiments were carried out with different metals (steel [1], grey iron [2], ductile iron [3], and aluminum [4,5]) and bonded sands (sodium silicate [2–4], furan [5], and green sand [2–4]). Monroe and Beckermann [6] studied the effect of mold restraint on hot tears by casting a T-shaped bar in a no-bake sand mold.

In contrast to mold restraint, mold expansion occurs at early casting times, shortly after filling. Because the casting is mostly liquid, the sand mold can easily expand into the mold cavity and reduce the casting volume. Peters et al. [7] studied the effect of cores on casting distortions through casting experiments in which a hollow cylinder was produced using silica and zircon sand cores.

**CONTACT** C. Beckermann becker@engineering.uiowa.edu

Through a finite element stress analysis, distortions were attributed to thermal expansion of the bonded sands as well as core restraint.

Computational advances in recent years have stimulated the development of complex constitutive models capable of predicting distortions and pattern allowances for castings of arbitrary size and shape. The accuracy of such models, however, remains uncertain, due in part to the limited availability of realistic mechanical properties and model parameters. This is particularly true at high temperatures where the majority of distortions can be expected to occur. These deficiencies have spurred researchers to study high-temperature properties of bonded sands, including compressive strength [8,9], tensile strength [9], and elastic modulus [10]. Since bonded sand is a multi-phase material containing sand grains, binder, and air voids, it should be modeled using a constitutive law that considers pressure-dependent yielding. This added complexity introduces extra parameters that must be determined through additional testing. The only high-temperature parameters for such models were determined by Saada et al. [11] who performed triaxial, uniaxial compression, isotropic compression, and die pressing tests on green sand at elevated temperatures to determine parameters for Cam Clay and Hujex constitutive models.

The mechanical tests from the previous studies provide invaluable data that is necessary to perform stress analyses for industrial casting processes. However, due to the extreme conditions encountered during casting, data acquired from laboratory tests may be unsuitable for the prediction of casting stresses and strains. In particular, the high heating rates near the mold-metal interface cannot be recreated by traditional mechanical testing. Thole and Beckermann [10] reported significant variations in the elastic modulus for heating rates ranging from 0.8 to 8 °C/min. In reality, however, heating rates in the bonded sand within a few millimeters of the mold-metal interface can reach several 100 °C/min. For this reason, the development of computational casting models using data from *in situ* experiments is preferable to using data from mechanical testing.

In this study, casting experiments are performed and then simulated in order to predict distortions and pattern allowances in steel sand castings. For the experiments, a thick-walled hollow steel cylinder is cast in a sand mold to measure distortions created by core expansion. The cores are constructed from two sands, silica and zircon. During the experiments, the temporal evolution of casting's inner diameter is measured *in situ* by utilizing LVDTs (Linear Variable Differential Transformers) connected to fused quartz rods. Temperatures are recorded in both the mold and casting using thermocouples. For the simulations, distortions and pattern allowances are predicted using a sequential temperature-displacement coupling, in which temperatures are calculated first using casting simulation software and then inputted into a finite element stress analysis. The steel is modeled using an elasto-visco-plastic constitutive law, whose parameters were calibrated in a previous study [12]. The bonded sands are modeled using the Drucker–Prager Cap constitutive law. Mechanical properties for the bonded sand are taken from the literature or estimated through room temperature mechanical testing. Through this procedure, the present study determines the mechanisms responsible for distortions caused by mold expansion. The present paper greatly expands on a preliminary conference publication by the same authors [13].

## 2. Description of experiments

### 2.1. Experimental setup

The casting geometry consisted of a thick-walled cylinder with dimensions (in mm) shown in Figure 1(a). A schematic of the experimental design is depicted at the vertical casting mid-plane in Figure 1(b). A core was utilized to create the hollow section of the cylinder and was held in place with a core print. The temporal evolution of the inner diameter at the mid-height of the cylinder was

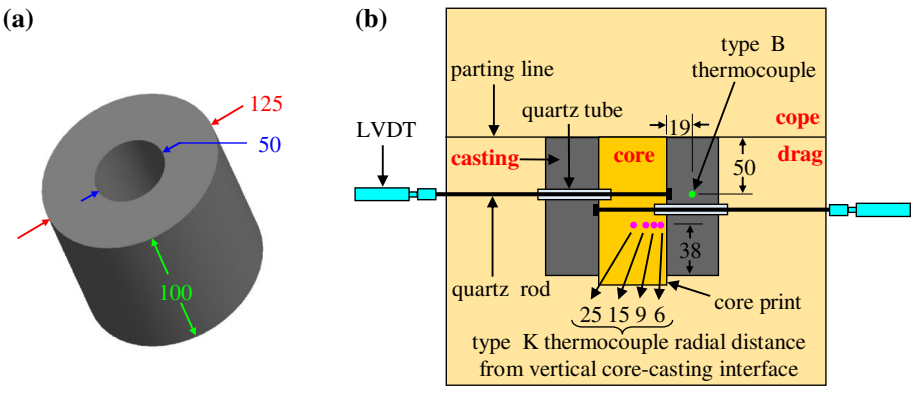


**Figure 1.** Casting geometry (a) and experimental schematic (b) for the cylinder experiments.
Note: All dimensions in mm.

measured by utilizing two identical assemblies consisting of a quartz rod, quartz tube, and LVDT. One end of the quartz rod was flattened into a disc (approximately 7 mm in diameter) using an oxy-acetylene torch and inserted through pre-drilled holes in the drag and core. The disc was butted to the outer diameter of the core, as shown in Figure 1(b). In order to transmit displacement, the quartz rod passed through a quartz tube, which traversed the mold cavity. The other end of the quartz rod was attached to an LVDT, which measured the displacement from one side of the inner diameter at a sampling rate of 2 Hz. The other assembly measured displacement on the opposite side of the cylinder. The LVDT measurements were added together to calculate the temporal evolution of the inner diameter. It is obvious from Figure 1(b) that both LVDT measurements could not be taken at the same height. Therefore, one measurement was taken approximately 5 mm above the cylinder mid-height, while the other was taken 5 mm below the mid-height.

Temperatures were measured at several locations. Type K thermocouples were inserted through the bottom of the drag and into the core at radial distances of 6, 9, 15, and 25 mm from the vertical core-casting interface. The thermocouples were staggered circumferentially to minimize the influence from other thermocouples. A type B thermocouple was encased in a quartz tube and inserted into the mold cavity to measure the temperature of the steel.

To build the cope and drag, Unimin® IC55 silica lake sand was bonded with a phenolic urethane no-bake (PUNB) binder system. The binder (1.25% of mold weight) was mixed using a 55:45 ratio of part 1 (PEPSET® 1000) to part 2 (Techniset® 6435). The cores were produced from either Unimin® IC55 silica lake or zircon sand and bonded using the same binder system as the cope and drag. The cope and drag were hand packed, whereas the cores were manually rammed. The core weights varied less than 1% for each type of core sand.

In total, 5 cylinders of each core type were produced (10 cylinders in total). For the first 4 cylinders, the inner diameter evolution was measured, as well as temperatures in the steel and at the 25 mm location in the core. For the final cylinder of each core type, no displacement or temperatures in the steel were recorded; only temperatures at the 4 core locations shown in Figure 1(b) were measured.

### 2.2. Casting procedure

Experimental casting trials were performed at the University of Northern Iowa's Metal Casting Center. The target chemistry was ASTM A216 grade WCB carbon steel. The castings were poured from a 250 lb heat and prepared in an induction furnace. The molten steel was heated to approximately 1700 °C in the furnace. The castings were poured within four hours after building the molds. Immediately before pouring, any slag was removed from the ladle. Rather than utilizing a pouring cup and sprue, the liquid steel was poured directly into the mold cavity, after which the cope was placed on top of the drag. This method was utilized to avoid additional mold-metal interactions from the sprue. For this reason, the mold cavity was never completely filled, resulting in an air gap (approximately 5 mm) between the casting and cope.

### 2.3. Experimental results

The changes in the inner diameter measured by the LVDTs are plotted in Figure 2(a) and (b) on complete and 600 s time scales, respectively. The complete time scale (40000 s) represents the approximate time needed to cool the casting to room temperature. Shortly after the onset of filling ($t = 0$), the inner diameters for the silica cores expanded to a maximum value (ranging from 1.15 to 1.3 mm) after 200 s. For the zircon core experiments, the inner diameters in experiments 1 and 2 expanded at approximately the same rate as the silica cores during the initial 25 s, whereas minimal expansion was measured in experiments 3 and 4 during this period. After 25 s, minimal additional expansion was measured for all zircon core experiments, as the curves are nearly horizontal

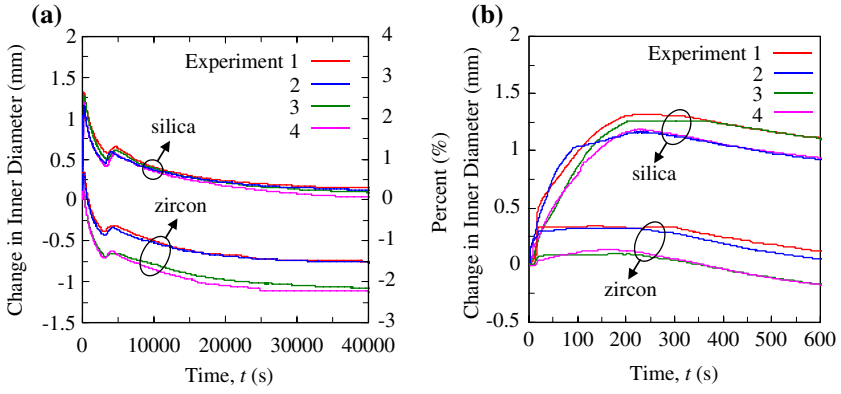


**Figure 2.** Measured change in the inner diameter at the cylinder's mid-height for the silica and zircon core experiments plotted on complete (a) and 600 s (b) time scales.

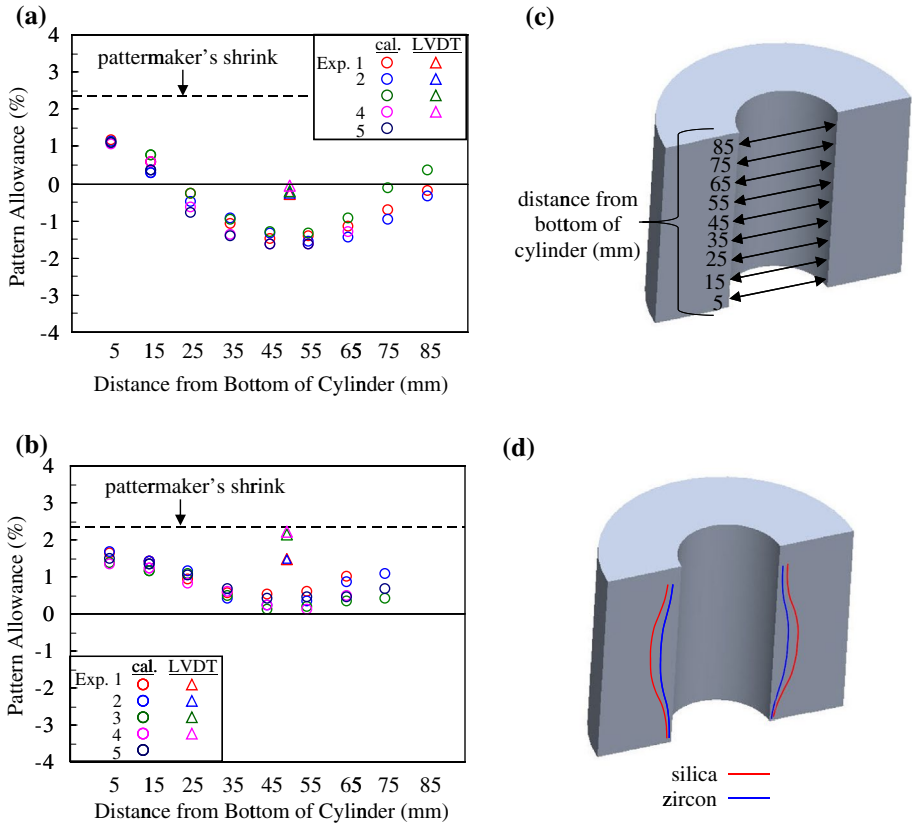


**Figure 3.** Pattern allowances were measured for the silica (a) and zircon (b) core experiments at the feature locations shown in (c). The measurements revealed barrel-shaped inner diameter profiles (d).

until 250 s. In general, the zircon cores expanded far less than the silica cores, which can be attributed to differences in the thermal expansion coefficients. This is partly due to phase transformations in silica sand that generated considerably more thermal expansion than zircon. At approximately 250 s, the inner diameters for all experiments (silica and zircon) began to contract, as solidification neared completion and thermal contractions commenced in the steel. As a result, the inner diameters decreased until a local minimum at approximately 4000 s and then increased until a local maximum at about 5000 s. This 'wiggle' is a manifestation of the volumetric expansion in the casting that accompanies the solid state phase transformation from austenite to pearlite and $\alpha$-ferrite. After 5000 s, the inner diameters decreased until room temperature. After 250 s, it is evident that all curves in Figure 3 contract (or expand during the phase transformation) at the same rate, i.e. all curves are parallel. In addition, the measured inner diameter contraction in the period $250 < t < 40{,}000$ s is equal to the pattern-maker's shrink for steel. These observations suggest that only thermal strains (i.e. no distortions) contributed to the LVDT measurements after 250 s. This is indeed the case and will be validated by the thermal strain predictions in Section 4 (see below). From this result, it can now be concluded that all distortions were generated by core expansion before solidification had completed. Core restraint did not create any distortions.

In addition to the LVDT measurements, pattern allowances for the inner diameters were measured using Equation (1) and are shown for the silica and zircon cores in Figure 3(a) and (b), respectively. The core (rather than pattern) dimensions were used to calculate pattern allowances. Measurements were taken with digital calipers at the feature locations shown in Figure 3(c). The pattern allowances are shown as circular symbols, with each color representing a different experiment. Any feature locations that contained large cracks or defects are not included in the figures. Each pattern allowance is the average of 16 measurements, taken circumferentially about the cylinder's inner diameter. Scatter in the plots can be attributed to surface roughness of the casting and possibly slight differences in the core bulk densities. The average standard deviation for the measurements was approximately 0.15 mm (0.3% *PA*). The dashed horizontal lines in Figure 3(a) and (b) denote the patternmaker's shrink of the steel (~2.3% for a circular geometry) and serve as a reference; distortions are quantified as deviations from this line. In general, the silica cores distorted more than the zircon cores, i.e. the silica core pattern allowances are smaller than those for the zircon cores. As in the LVDT measurements, these differences can again be attributed to differences in thermal expansion coefficients. The largest core expansions (for both silica and zircon cores) were observed at the mid-height of the cylinder, while smaller expansions occurred near the ends.

As a result, the inner diameter of the cylinder evolved into a barrel-shaped profile (see Figure 3(d)), which can be explained by the local solidification times. At early casting times, the steel was mostly liquid and provided little restraint. As a result, the core easily expanded into the mold cavity. The solid fraction increased until eventually the steel reached coherency, which was accompanied by a dramatic increase in strength that prevented any further mold expansion. Since the inner diameter near the top and bottom of the cylinder solidified before the mid-height inner diameter, the largest expansion occurred at the mid-height.

Another observation from Figure 3 is that a large amount of scatter can be seen in the pattern allowances near the top of the cylinder. Recall that the mold was filled by pouring molten steel directly into the mold cavity (i.e. no gating system was used). In order to prevent spilling steel on the foundry floor, the mold cavity was never completely filled, which resulted in an air gap between the casting and cope. The thickness of this gap varied somewhat among the experiments, which affected cooling rates and the associated times to coherency.

Pattern allowances at the mid-height of the cylinder can also be calculated from the LVDT measurements by replacing the numerator in Equation (1) with the negative change in the inner diameter at 40000 s (see Figure 2(a)). These values are shown as triangular symbols in Figure 3(a) and (b). Unfortunately, a discrepancy can be seen between the LVDT and calipers pattern allowances, as the LVDT values are higher than those from the calipers. In other words, the calipers measured more core expansion than the LVDTs. The repeatability of the LVDT measurements after 250 s (see Figure 2) suggests they are correct (this will be validated by the thermal strain simulations in Section 4). Therefore, the discrepancy must have occurred during the initial 250 s. Most likely, the quartz rods were not embedded in the mostly liquid steel at early times and 'slipped'. As a result, some amount of core expansion was not measured by the LVDTs. To remedy this, the LVDT measurements in Figure 3 were shifted upwards so that the LVDT and calipers pattern allowances coincided. The adjusted curves are shown in Figure 4. Note that the circular symbols on the secondary vertical axis in Figure 4(a) represent the calipers measurements. Then, the LVDT curves were modified during the initial 100 s to smoothly increase from zero to the shifted measurements. These modifications are shown as dashed lines in Figure 4(a). The resulting curves will be used below to validate the stress model predictions.

## 3. Thermal simulations

Temperatures in the casting, mold, and core were calculated using the commercial casting simulation software MAGMASOFT® [14]. Thermophysical properties (i.e. density, specific heat, thermal conductivity) for the mold, as well as heat transfer boundary conditions, were taken from the MAGMASOFT® database, whereas the thermophysical properties, solid volume fraction, and latent heat of fusion for the steel were calculated using IDS [15] software. With the exception of the latent heat, all properties are temperature-dependent.

Using the estimated properties, the predicted temperatures did not agree with the thermocouple measurements. To match the predicted and measured temperatures, several properties were adjusted through a trial-and-error process. The complete procedure is described in detail elsewhere [16,17]. The main modifications were made to the thermal conductivity for the bonded sands and latent heat of fusion for the steel. After the adjustments, the predicted and measured temperatures for the silica and zircon core experiments were in excellent agreement at all times (see Figure 5(a) and (b)). Very little difference was observed between the measured temperatures from the zircon and silica core experiments. Therefore, a single set of transient temperature fields can be used to predict distortions for the zircon and silica core experiments. Predicted solid fraction contours (shown at 25 s, 50 s, 100 s, and 200 s) in Figure 5(c) demonstrate the uneven solidification in the cylinder that led to the barrel-shaped profile of the inner diameter.

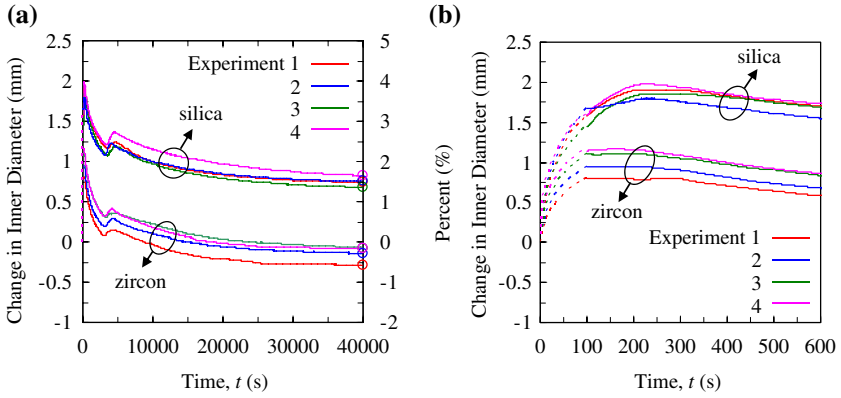


**Figure 4.** Adjusted LVDT measurements. The LVDT curves in Figure 2 were modified to match the pattern allowance measurements, which are represented by the circular symbols on the secondary axis in (a) Complete Time Scale (b) 600s time scale.

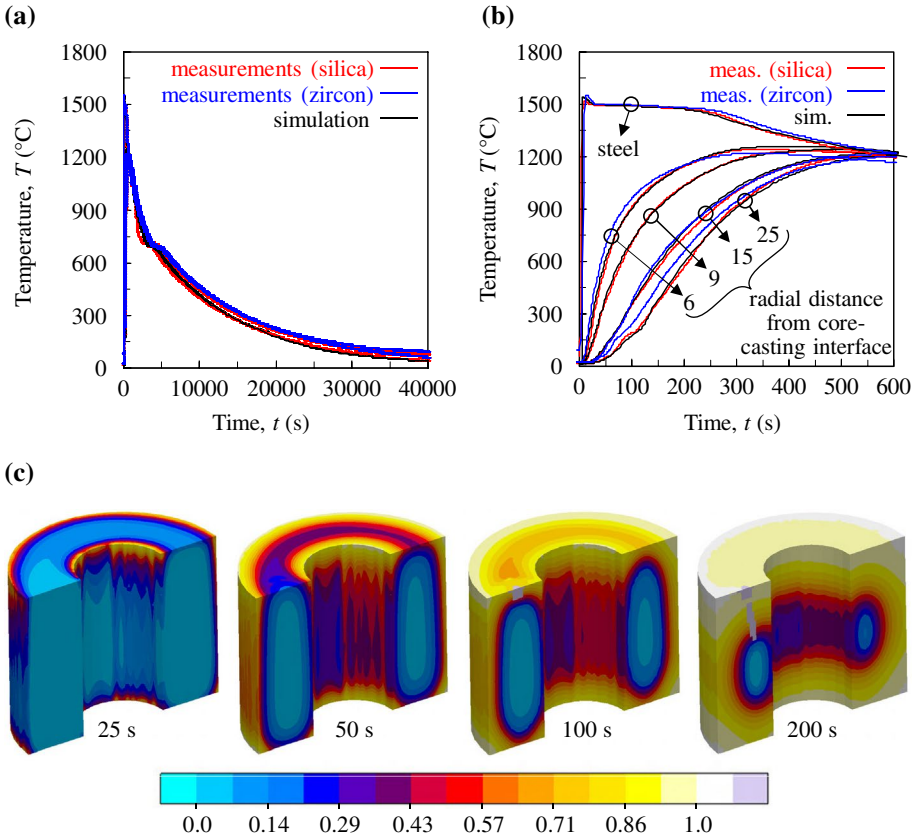


**Figure 5.** Comparison between measured and predicted temperatures for the silica and zircon core experiments on complete (a) and 600 s (b) time scales. The thermocouple at the 9 mm location for the zircon core experiment failed. Solid Fraction contours (c) illustrate uneven solidification.

The predicted temperature fields were saved at a sufficient number of time steps (approximately 100) to ensure a smooth temperature profile at all nodes. The results were then mapped to the finite element mesh used in the stress analysis using MAGMAlink, a built-in functionality within MAGMASOFT® that enables temperatures to be easily transferred to finite element codes.

## 4. Thermal strain predictions

Preliminary finite element simulations were used to predict the evolution of thermal strains in both the casting and core. The importance of these simulations is twofold. First, the predicted thermal strains in the casting can be subtracted from the LVDT measurements to reveal the evolution of casting distortions. Second, the predicted thermal strains in the core will verify whether thermal expansion of the bonded sand can account for the cylinder's inner diameter expansion during solidification. If not, another mechanism must be considered. Two simulations were performed, in which the casting and core were simulated separately. Minimal boundary conditions were enforced to prevent rigid body translations and rotations.

The predicted change in inner diameter for the steel cylinder due to thermal strains is compared with the silica and zircon LVDT measurements on complete and 600 s time scales in Figure 6(a) and (b), respectively. The temperature dependent linear thermal expansion coefficient of the steel (shown in Figure 6(c)) was calibrated by Galles and Beckermann [12] and the steel was set to begin thermally contracting at $g_s = 0.97$ [12]. During the initial 250 s, the thermal strain simulation curve is horizontal, as no changes in the inner diameter were predicted. Beginning at 250 s, thermal contractions commenced in the steel and reduced the inner diameter, which can be seen as a decrease in the thermal strain simulation curve. From $t = 250$ s until the onset of the solid state phase transformation (at approximately 4000 s), the thermal strain simulation curve decreases at the same rate as the silica and zircon LVDT measurements. The kink in the linear thermal expansion curve at approximately 700 °C (see Figure 6(c)) is included to predict the volumetric expansion associated with the phase transformation. After the transformation, the thermal strain prediction curve decreases at the same rate as the LVDT measurements. It is obvious that the measured and simulated curves are parallel after 250 s. This verifies the previous assertion that all changes in the inner diameters after 250 s were created by thermal strains in the solidified steel. Hence, to reiterate, all casting distortions in this study were created by core expansion during solidification. Core restraint after solidification did not generate distortions.

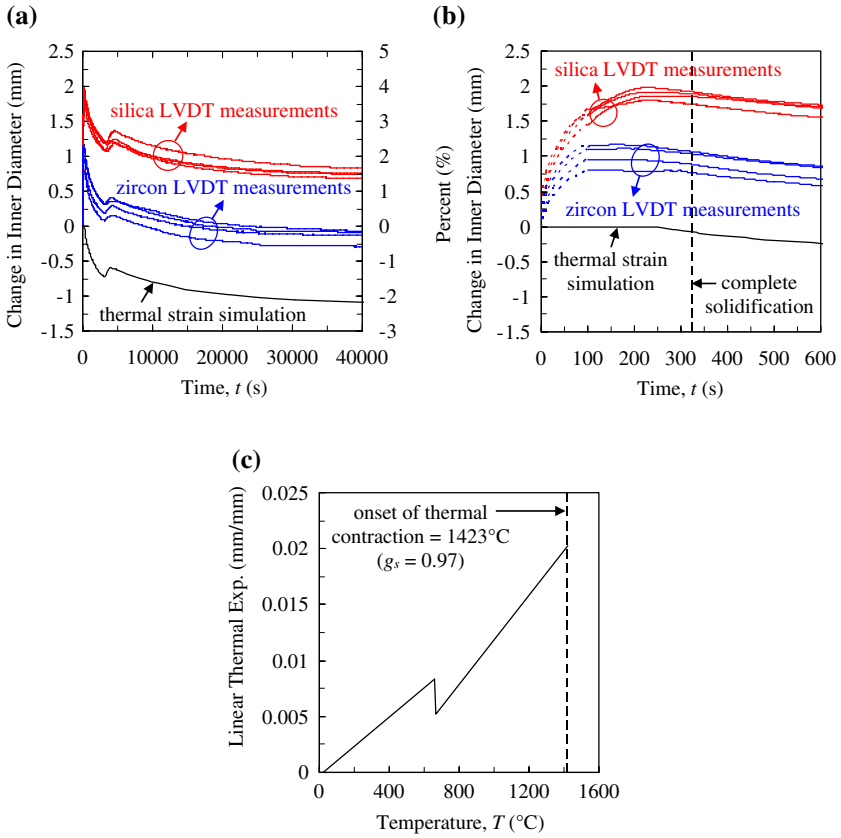


**Figure 6.** Comparison between the LVDT measurements and predicted thermal strains in the cylinder on complete (a) and 600 s (b) time scales. Thermal strains were calculated using the linear thermal expansion coefficient in (c), which was calibrated by Galles and Beckermann [12].

The predicted thermally induced change in the diameter for the silica and zircon cores at mid-height are compared to the LVDT measurements on complete and 600 s time scales in Figure 7(a) and (b), respectively. Thermal strains in the cores were calculated using the temperature dependent linear thermal expansion coefficient in Figure 7(c), which was measured in separate experiments using a dilatometer. The curves in Figure 7(c) illustrate the vast difference in thermal expansions between the different sands. In particular, phase changes in silica sand at 560 and 1470 °C generate considerable expansion, whereas no such events occur in zircon sand. In general, the predicted core expansions greatly under-predicted both the silica and zircon LVDT measurements. For example, the simulation only predicted a 0.5 mm (roughly 25% of the measurement) increase in diameter for the silica core after 200 s. Similarly, the predicted expansion at 200 s for the zircon core (~0.1 mm) is far less than the measured inner diameter expansions, which ranged from 0.75 to 1.25 mm. After approximately 8000 s, the outer diameters for the silica and zircon cores begin to thermally contract until the predicted changes in core diameters were reduced to zero at room temperature (40,000 s). These contractions, however, have no influence on the pattern allowances in the cylinder, as distortions were only generated during the initial 200 s.

Such large discrepancies between the measurements and predictions during the initial 200 s suggest that another mechanism contributed to the cylinder's inner diameter expansion. Initially, it was postulated that the cristobalite phase transformation in silica sand (see the sharp increase at approximately 1470 °C in Figure 7(c)) may have been affected by atmospheric conditions inside the core, which in turn caused the transformation to occur at a lower temperature. Unfortunately, this argument cannot be made for the zircon core experiments because zircon sand does not experience phase changes. However, at the time, the zircon core experiments had yet to be performed. Therefore, through a parametric study, it was found that the measured inner diameter expansion could be predicted by reducing the cristobalite transformation temperature to 1300 °C. Based on this result, a new experiment was designed as depicted in Figure 8(a). A rectangular plate (300 mm length × 38 mm thickness × 150 mm depth) was cast in a silica sand mold. Bonded sand samples were packed in thin-walled quartz tubes (25 mm inner diameter and 1 mm wall thickness) that were inserted through predrilled holes in the bottom of the drag so that the top of the tubes were positioned flush with the bottom of the mold cavity. The mold was filled using a simple gating system that consisted of a pouring cup and sprue.

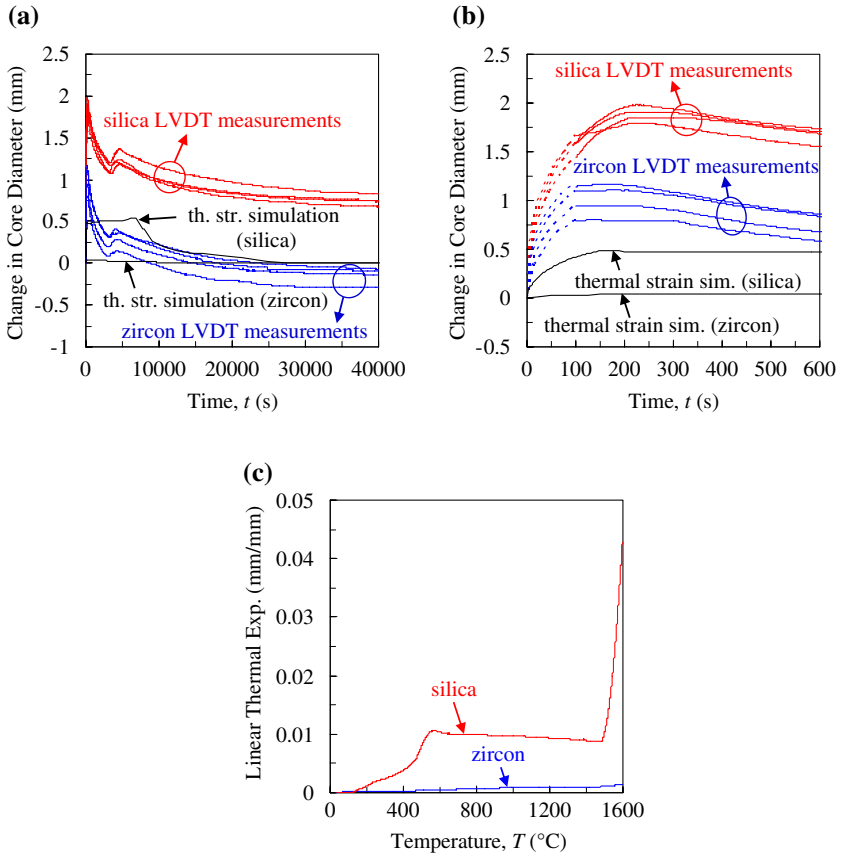


**Figure 7.** Comparison between the LVDT measurements and predicted thermal strains in the silica and zircon bonded sands on complete (a) and 600 s (b) time scales. Thermal strains were predicted using the measured linear thermal expansions in (c).

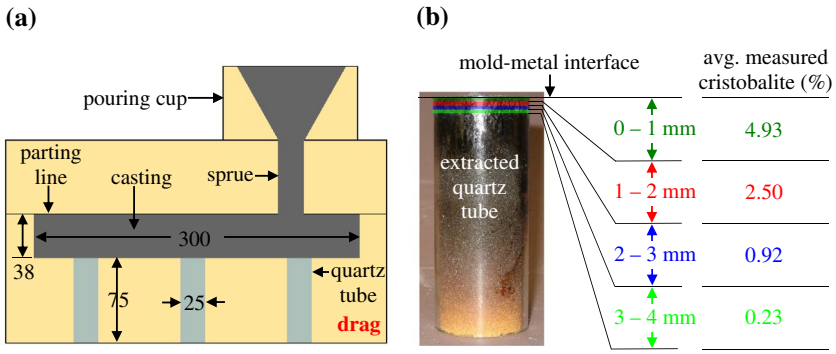


**Figure 8.** Experimental setup (a) used to measure the formation of cristobalite in bonded silica sand. Layers of sand were removed in 1 mm layers from the extracted quartz tube in (b) and tested using X-ray diffraction.
Note: All dimensions in mm.

After the casting cooled to room temperature, the quartz tubes were carefully extracted from the mold. The bonded sand was then removed in 1-mm thick layers (see Figure 8(b)) and tested using X-ray diffraction. Cristobalite is quasi-stable at room temperature, as kinetic barriers prevent its transformation back to quartz [18]. From the samples, the closest 1 mm layer from the mold-metal interface was found to contain less than 5% of the cristobalite phase. Smaller amounts were found in subsequent layers, as shown in Figure 8(b). These small amounts of cristobalite could only account for about 0.01 mm of additional expansion in the experiment. Therefore, the unexplained core expansion in the silica core experiments could not be explained by cristobalite formation.

A plausible explanation is that sand dilation caused the unexplained core expansion. Dilation is illustrated in Figure 9; the initial state of dense sand contains small air voids between the grains (Figure 9(a)). After a shear force is applied, however, the irregularly-shaped sand grains translate and/or rotate and cause the voids to grow, resulting in volumetric expansion of the sand aggregate (Figure 9(b)). The rapid flow of heat from the casting heats the refractory core from the outside

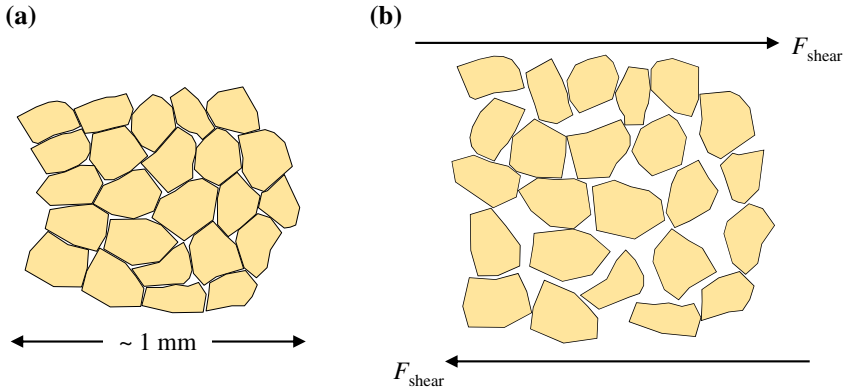


**Figure 9.** Dense sand dilates (i.e. volumetrically expands) when subjected to a shear force, $F_{shear}$, due to void growth between grains (a) Initial State of Dense Sand (b) Dilated State.



inward, generating large temperature gradients. This uneven heating is conducive to the formation of shear forces. Saada et al. [11] suggested that dilatant behavior occurred for temperatures greater than 120 °C. For this study, the Drucker–Prager Cap model features the ability to predict dilation.

## 5. Stress model and mechanical properties

### 5.1. Governing equations

The stress model solves for the evolution of stresses and displacements in the casting, core, and mold from the onset of filling until shakeout. The small strain assumption is adopted for the present study. Assuming negligible inertial effects, body forces, and momentum transport between the solid and liquid during solidification, the solid momentum equation is reduced to a zero divergence of the stress tensor ($\boldsymbol{\sigma}$), i.e. $\nabla \cdot \boldsymbol{\sigma} = 0$. The strain tensor ($\boldsymbol{\varepsilon}$) is additively decomposed into its elastic ($\boldsymbol{\varepsilon}_e$), inelastic ($\boldsymbol{\varepsilon}_{in}$), and thermal ($\boldsymbol{\varepsilon}_{th}$) components.

### 5.2. Constitutive Model and Mechanical Properties for the Steel

The constitutive model for the steel is based on the implementation by Monroe and coworkers [19,20], in which the mushy zone is treated as a compressible porous medium. In addition, the model considers rate, hardening, and temperature effects. The yield stress is defined as a function of the solid volume fraction, which eliminates the need to model each phase (i.e. fully liquid, fully solid, semi-solid) separately. The coherency solid fraction, $g_s^{coh}$, represents a transition; below $g_s^{coh}$, the steel has no tensile strength and is modeled as an elastic material with a low modulus. Above $g_s^{coh}$, the dendrites form a continuous network, allowing the steel to transmit stresses. For the present study, a parametric study found that the finite element predictions were insensitive to changes in $g_s^{coh}$ from 0.3 to 0.8. For $g_s = 1$, the model reduces to a standard elasto-visco-plastic constitutive law. A detailed description of the model, including the determination of the mechanical properties, is given by Galles and Beckermann [12].

### 5.3. Constitutive Model for Bonded Sand

For this study, the stress analysis was performed using the general purpose finite element code ABAQUS® [21]. Several models in the ABAQUS® material library can be used to model granular media that exhibit pressure-dependent yielding. The Cam-clay model was dismissed based on its tendency to over-estimate yield stresses on the 'dry side' of the failure surface for cohesionless materials (i.e. dry sand), as well as its inability to predict the observed softening and dilatancy in dense sands [22]. The Mohr–Coulomb model in the ABAQUS® library does not employ a cap and, therefore, cannot predict compaction. Based on these limitations, the bonded sands used in the mold and core were modeled using the Drucker–Prager Cap model, which is reviewed here for completeness.

The Drucker–Prager Cap model is defined by a multi-surface yield function, shown in the meridional (i.e. deviatoric stress vs. pressure) plane in Figure 10(a). The shear failure ($F_s$) surface is defined as

$$F_s = t - p\tan\beta - d = 0 \tag{2}$$

where, $p = -1/3\ \text{trace}\,(\boldsymbol{\sigma})$ is the pressure and $\tan\beta$ is the slope of the failure surface. The cohesion parameter ($d$), defines the intersection of the shear failure surface with the deviatoric stress axis. The deviatoric shear stress ($t$) is given as

$$t = \frac{1}{2}q\left[1 + \frac{1}{K} - \left(1 - \frac{1}{K}\right)\left(\frac{r}{q}\right)^3\right] \tag{3}$$

In Equation (3), $q = \sqrt{3/2(\boldsymbol{\tau}:\boldsymbol{\tau})}$ is the von Mises stress and determined from the deviatoric stress tensor, $\boldsymbol{\tau} = \boldsymbol{\sigma} + p\boldsymbol{1}$, where $\boldsymbol{1}$ is the second order identity tensor. Also, $r = (9/2\boldsymbol{\tau}:\boldsymbol{\tau}\cdot\boldsymbol{\tau})^{1/3}$ is the third stress invariant, and $K$ governs the shape of the yield surface in the deviatoric stress plane (see Figure 10(b)). For the present study,

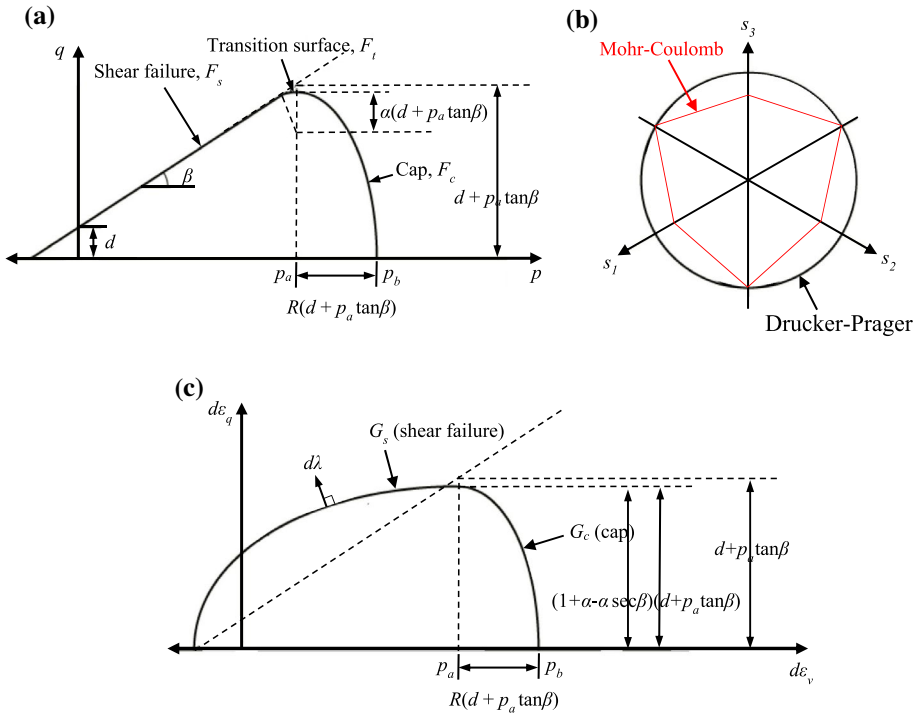


**Figure 10.** The Drucker–Prager Cap yield surface shown in the meridional (a) and deviatoric (b) planes. The plastic potential (c) uses associated and non-associated flow rules for the cap and failure surfaces, respectively.

$K = 1$ (i.e. a circle in the deviatoric plane) is required for ABAQUS®/explicit, which reduces Equation (3) to $t = q$. The Drucker–Prager yield surface is taken to circumscribe the Mohr–Coulomb failure envelope in the deviatoric stress space.

The cap ($F_c$) and transition ($F_t$) surfaces in Figure 7(a) are defined, respectively, as

$$F_c = \sqrt{[p - p_a]^2 + \left[\frac{Rt}{(1 + \alpha - \alpha/\cos\beta)}\right]^2} - R(d + p_a \tan\beta) = 0 \quad (4)$$

and

$$F_t = \sqrt{[p - p_a]^2 + \left[t - \left(1 - \frac{\alpha}{\cos\beta}\right)(d + p_a \tan\beta)\right]^2} - \alpha(d + p_a \tan\beta) = 0 \quad (5)$$

where $R$ is the eccentricity of the elliptical cap, $\alpha$ is a small number (typically 0.01 to 0.05) that defines the shape of the transition surface, and the evolution parameter ($p_a$) is defined as

$$p_a = \frac{p_b - Rd}{(1 + R\tan\beta)} \quad (6)$$

where $p_b$ is the hydrostatic compressive strength and defines the intersection of the cap with the pressure axis in Figure 10(a). The hardening/softening behavior is governed by the evolution of $p_b$ with plastic volumetric strain increments and was determined for this study with a 1-D compression test (see Section 5.4).

The plastic strain increment ($d\boldsymbol{\varepsilon}_{pl}$) is determined from the flow rule, given as

$$d\boldsymbol{\varepsilon}_{pl} = d\lambda \frac{\partial G}{\partial \boldsymbol{\sigma}} \quad (7)$$

In Equation (7), $d\lambda$ is the magnitude of the plastic strain increment, $G$ is the plastic potential, and $\partial G/\partial \boldsymbol{\sigma}$ is the direction of the plastic flow. The plastic potentials for the failure surface ($G_s$) and cap surface ($G_c$) are shown in Figure 10(c) and given as

$$G_s = \sqrt{\left[(p_a - p)\tan\beta\right]^2 + \left[\frac{t}{(1 + \alpha - \alpha/\cos\beta)}\right]^2} \quad (8)$$

and

$$G_c = \sqrt{[p_a - p]^2 + \left[\frac{Rt}{(1 + \alpha - \alpha/\cos\beta)}\right]^2} \quad (9)$$

Note that in Equations (8) and (9) no new parameters have been defined. The parameters used to characterize the yield surface also define the plastic potential. Comparing Figure 10(a) and (c), it is obvious that $F_c = G_c$, which implies associated flow in the cap region. For the shear failure region, a non-associated flow rule is used, as the yield surface is different from the plastic potential. This is typical for materials that exhibit dilative behavior.

### 5.4. Properties for bonded sands

In this study, core expansion was induced by high heating rates near the mold-metal interface, which suggests the high-temperature mechanical properties play an important role for predicting distortions. Unfortunately,

no commercially available mechanical testing machines possess the necessary high-temperature measurement capabilities. Consequently, no high-temperature mechanical testing was performed in this study. Instead, as a first estimate, the high-temperature mechanical properties of the bonded sands were determined from room temperature tests on un-bonded, densely-packed sands. Using un-bonded sand to estimate properties is reasonable because pyrolysis of the binder essentially reduced the molds and cores to un-bonded sands at high temperatures.

Several properties ($\beta$, $\alpha$, $R$, $\nu$) were set to constant values for all temperatures. Based on the findings of Saada et al. [11], the friction angle ($\beta$) was held constant. The shape parameter for the transition surface ($\alpha = 0.01$) only governs a small portion of the yield surface and will have little impact on the simulation results. The eccentricity ($R$ = 0.45 [23]) defines the ratio of the major to minor axis for the elliptical cap surface. Due to the limited data available in the literature, this value was taken as a constant. Poisson's ratio ($\nu = 0.3$) was also taken as a constant.

The remaining properties ($E$ and $d$) were estimated over the entire casting temperature range using the following procedure. The room temperature bonded sand properties were linearly decreased to their high-temperature values at some critical temperature, $T_{crit}$, and then held constant for all $T > T_{crit}$. The critical temperature represents the onset of pyrolysis of the binder, after which the mold and core are transformed to un-bonded sands. Although the properties can be expected to exhibit some degree of temperature dependency above $T_{crit}$, such variations are likely minimal over the temperature range for which distortions occurred. Therefore, using constant values above $T_{crit}$ is a reasonable first estimate.

A single temperature dependent Young's modulus ($E$) was used for the silica and zircon bonded sands. The room temperature ($E_{R.T.}$ = 3403 MPa) and high temperature ($E_{H.T.}$ = 60 MPa) values were taken from Thole and Beckermann [10] and Hettler and Vardoulakis [24], respectively.

The shear failure surface parameters ($\beta$ and $d_{H.T.}$) for the Drucker–Prager Cap model were estimated from drained triaxial compression tests. An un-bonded cylindrical test specimen (70 mm long and 38 mm diameter) was contained in a 1-mm thick elastomer membrane during the test and housed in a triaxial cell. The test was carried out in 2 steps. First, a confining pressure was applied by filling the triaxial cell with water and then pressurizing it. This created a hydrostatic stress state, i.e. $\sigma_1 = \sigma_2 = \sigma_3$ (where the subscripts denote the principal directions. As is customary for geological materials, compressive stresses are defined here as positive values). Next, a displacement-controlled piston compressed the test specimen in the axial direction at a constant rate of 0.01 mm/min until a peak axial force ($F$) was measured. The peak axial stress, $\sigma_1$, was calculated by dividing the peak axial force by the cross-sectional area of the specimen and adding the result to the confining pressure, i.e. $\sigma_1 = F/A + \sigma_3$. In total, 5 tests were performed for both sands, each at a different confining pressure (100, 200, 300, 400, and 600 kPa). For each test, a Mohr's circle can be constructed from the confining pressure, $\sigma_3$, and peak axial stress, $\sigma_1$. The friction angle can then be determined using the Mohr–Coulomb failure criterion. However, obtaining a best-fit failure envelope is difficult using this method. A convenient alternative is to plot the triaxial data on a modified Mohr–Coulomb diagram in which $1/2(\sigma_1 - \sigma_3)$ is plotted versus $1/2(\sigma_1 + \sigma_3)$. This diagram is advantageous because a single point represents each test, which enables a best-fit line to be easily constructed. Since dry sand has no cohesion, the cohesion parameter was set to zero by forcing the best-fit line through the origin. The results of the silica and zircon triaxial tests are shown on the modified Mohr–Coulomb diagram in Figure 11(a). The angles of the best-fit lines for the silica and zircon sand tests were found to be $\psi = 35°$ and 33°, respectively. Then, using the relation

$$\varphi = \sin^{-1}(\tan\psi) \tag{10}$$

the Mohr–Coulomb friction angles were calculated as $\phi = 45°$ and 40° for silica and zircon, respectively. Finally, the Drucker–Prager friction angle was calculated using the relation

$$\tan\beta = \frac{6\sin\varphi}{\sqrt{3}(3 - \sin\varphi)} \tag{11}$$

to give $\beta$ = 55° and 52° for silica and zircon, respectively. Conversion of the cohesion parameter from the modified Mohr–Coulomb diagram to the high temperature Drucker–Prager cohesion resulted in $d_{H.T.} = 0$ for both sands. Equation (11) assumes the Drucker–Prager yield surface circumscribes the Mohr–Coulomb failure surface in deviatoric space, as shown in Figure 10(b). The room temperature cohesion ($d_{R.T.}$) was estimated through a finite element stress analysis performed on a uniaxial tension test for bonded sand [9]. Starting at 1 MPa, $d_{R.T.}$ was incrementally increased until the maximum observed tensile strength could be predicted. This occurred at $d_{R.T.} = 1.85$ MPa. Since the Drucker–Prager Cap model in ABAQUS® predicts perfect plasticity in tension, the maximum predicted stress is also the yield stress.

Hardening/softening behavior for the Drucker–Prager Cap model is associated with plastic volumetric strains and was determined for both sands from room temperature 1-D compression tests. An un-bonded cylindrical test specimen (25.4 mm height and 38.1 mm diameter) was compressed in the axial direction at a rate of 0.254 mm/min. The sample was housed in a rigid ring to prevent displacement in the radial direction. Initial bulk densities ($\rho_{b0}$) were 1858 and 3169 kg/m$^3$ for the silica and zircon sands, respectively. Although the test

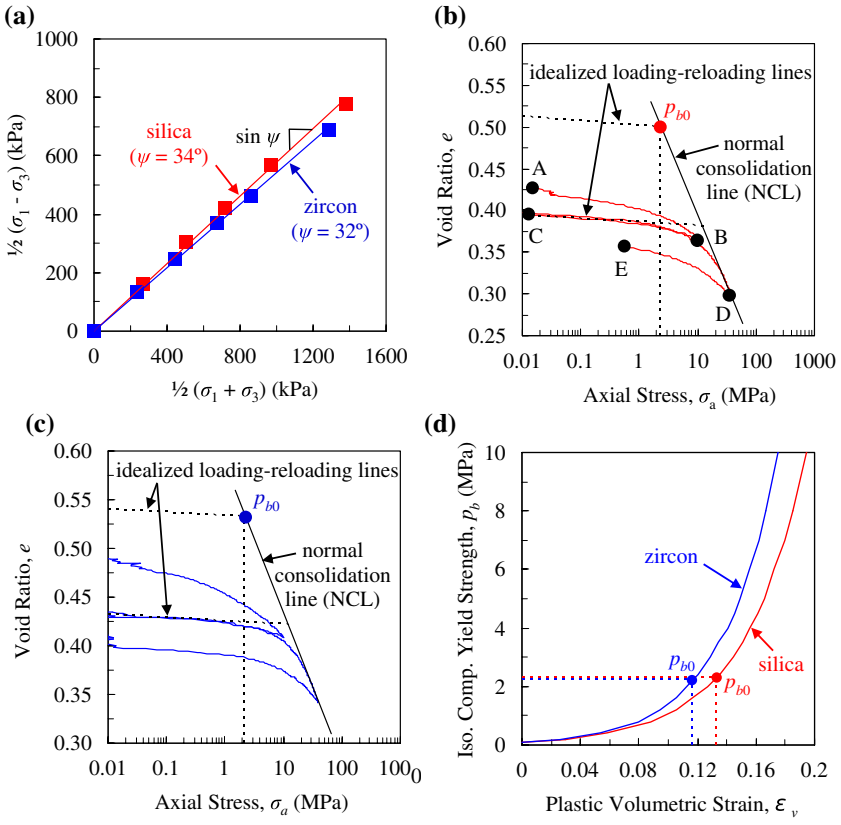


**Figure 11.** Friction angles ($\psi$) were determined from the Modified Mohr–Coulomb diagram (a). 1-D compression test results for silica (b) and zircon (c) sands were used to determine the hardening behavior (d).

specimens were not packed, their bulk densities were higher than the measured room temperature core bulk densities used in the experiments (1751 kg/m$^3$ for silica and 3062 kg/m$^3$ for zircon). These differences are attributed to the binder in the cores, which reduced the volume fraction of sand grains. 1-D compression test results are plotted as void ratio ($e$) vs. log $p$ for the silica and zircon sands in Figure 11(b) and (c), respectively. The void ratio is defined as the ratio of void volume ($V_v$) to solid volume ($V_s$) for the aggregate, i.e. $e = V_v / V_s$. The initial void ratio ($e_0$) is calculated from the initial bulk density using the relation $e_0 = \left(\rho_p / \rho_{b0}\right) - 1$ where $\rho_p$ is the particle density ($\rho_p$ = 2650 and 4700 kg/m$^3$ for silica and zircon respectively). The tests were carried out in the sequence (A-B-C-D-E) shown in Figure 11(b). The test specimen ($e_0$ = 0.424) was loaded in segment A-B, unloaded in B-C, loaded again in C-D, and unloaded in D-E. From this procedure, a family of nearly-parallel curves can be seen in Figure 11(b) and (c) at pressures less than 10 MPa. In particular, segment B-C contains one unloading line and one reloading line, and both follow the same path. This implies that the unloading-reloading lines characterize the elastic response of the sand. This segment was then used as a guide to generate an idealized loading-reloading curve, whose slope is assumed to be independent of the initial bulk density. The idealized loading-reloading curves were then shifted upward to correspond to the initial void ratios from the experiments (0.52 for silica and 0.54 for zircon).

The normal consolidation line (NCL) was determined from the slope of the 1-D compression curve at high pressures and assumed to be linear on log $p$. In order to include all pressures associated with sand casting, the curve was extrapolated to low pressures, as shown in Figure 11(b) and (c). The position of the cap (see Figure 10(a)) at the onset of casting represents the initial hydrostatic compressive strength, $p_{b0}$, and is determined by the intersection of the idealized loading-reloading line and the NCL in Figure 11(b) and (c). Any increase or decrease in $p_b$ from the initial state is constrained to lie on the NCL. The change in void ratio is calculated from the plastic volumetric strain increment ($\Delta\varepsilon_v^{pl}$) using the relation $\Delta\varepsilon_v^{pl} = \left(e_2 - e_1\right) / \left(1 + e_1\right)$, where the subscripts denote the initial (1) and final (2) states. Thus, the evolution of $p_b$ with $\Delta\varepsilon_v^{pl}$ defines the hardening/softening behavior for the bonded sands. This relation is plotted for both sands in Figure 11(d). It is clear from the figure that the compressive strength for zircon sand is higher than for silica sand.

## 6. Stress simulations

### 6.1. Procedure

Stress simulations were performed using the general purpose finite element code ABAQUS®/explicit. An explicit integration scheme was chosen to avoid convergence issues associated with material softening when

the material yields on the Drucker–Prager shear failure surface. The time step using the explicit method is conditionally stable. The critical time step is $\Delta t \leq 2/\omega_{max}$, where $\omega_{max}$ is the highest frequency (i.e. largest eigenvalue) of the system. This stability limit can be rewritten as

$$\Delta t = \min\left(\frac{L_e}{c_d}\right) \tag{12}$$

where is $L_e$ the characteristic element dimension and is derived from an analytic upper bound expression for the maximum element eigenvalue. The effective dilatational wave speed ($c_d$) of the material is defined as

$$c_d = \sqrt{\frac{\lambda + 2\mu}{\rho}} \tag{13}$$

In Equation (13), $\lambda = E\nu/[(1+\nu)(1-2\nu)]$ is the first Lamé constant, $\mu$ is the shear modulus, and $\rho$ is the material density.

Inputting the mold and steel properties into Equation (13) gives very large dilatational wave speeds that limit the time step and lead to impractical simulation times. For casting processes, however, inertial forces are not important, as deformations occur at rates much lower than the dilatational wave speed. Therefore, the time step may be significantly increased without affecting the simulation results. This is achieved in ABAQUS®/explicit through 'mass scaling' in which the mass is artificially increased. To ensure that mass scaling does not significantly affect the results, the ratio of kinetic energy to total energy in the simulation should not exceed 5%.

For the simulation model, the cope was excluded because it did not contact the steel during casting. Contact interactions between the casting, core, and drag were defined using the general contact algorithm in ABAQUS®/explicit, which employs a penalty method. Friction between the contact surfaces was found to have a negligible impact on distortions and set to zero. Zero displacement boundary conditions (i.e. $u_x = 0$, $u_y = 0$, $u_z = 0$) were specified on the bottom of the drag to prevent rigid body translations and rotations. First-order tetrahedral elements were used for the entire model. Taking advantage of symmetry, only 1/4 of the geometry was modeled. For the simulation model, the casting consisted of approximately 10,000 nodes and 50,000 elements, whereas the mold and core contained 17,000 nodes and 90,000 elements. A mesh sensitivity study, not shown here, revealed insignificant changes in the results



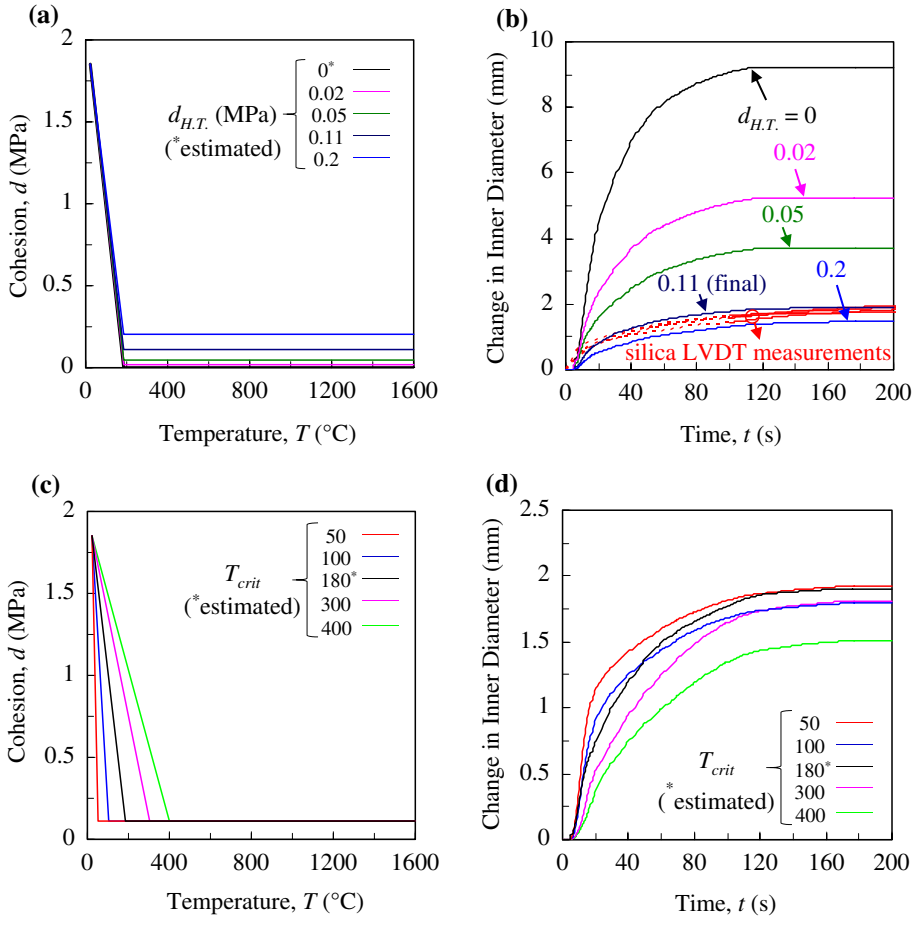


**Figure 12.** The high temperature cohesion parameter ($d_{H.T.}$), was adjusted as shown in (a) to match the simulated change in inner diameter to the LVDT measurements for the silica cores (b). A parametric study investigated the effect of changes in the critical temperature, $T_{crit}$, (c) on the predicted change in inner diameter (d).

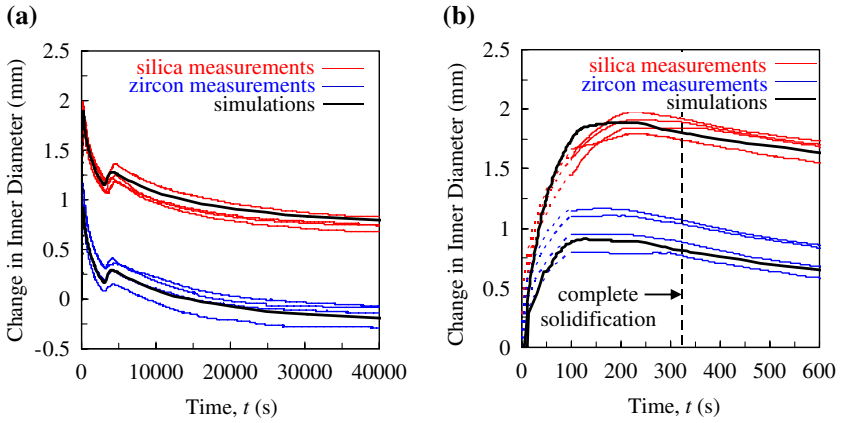


**Figure 13.** Comparison between measured and predicted changes in the inner diameter for the silica and zircon core experiments after adjusting the high temperature cohesion (a) complete time scale (b) 600 s time scale.



when using finer meshes. Simulations were performed on an Intel® Xeon® E5-2687W v2 processor containing 8 cores with a CPU clock speed of 3.4 GHz. Run times were approximately 2 h.

### 6.2. Stress simulations

The stress simulations required several inputs. The estimated elastic properties ($E$ and $v$), Drucker–Prager Cap parameters ($\beta$, $d$, $\alpha$, $R$), and hardening curves (see Figure 11(d)) for the bonded sands are described in Section 4.4. The initial hydrostatic compressive strengths ($p_{b0}$ = 2.4 and 2.3 MPa for the silica and zircon cores, respectively) were determined from the void ratio ($e$) vs. log $p$ plots (see Figure 11(b) and (c)) using the initial bulk density of the bonded sands. The elasto-visco-plastic properties for the steel were taken from Galles and Beckermann [12]. The thermal expansion coefficients for the steel and bonded sands are shown in Figures 6(c) and 7(c), respectively. Finally, the calculated temperature fields were inputted from MAGMGASOFT®.

Using the inputs, the finite element stress analysis predicted stresses and strains in the casting, core, and drag. For the initial simulation, excessive dilation was predicted and the simulated change in inner diameter far exceeded the LVDT measurements. This is in stark contrast to the free core expansions that only predicted a small fraction of the LVDT measurements (see Figure 7). In order to match the measured and simulated core expansions, parametric studies were performed to determine which parameter to adjust. Only the high temperature properties were considered, as negligible distortions can be expected at the lower temperatures. In order to avoid an arbitrary matching procedure, it was decided to adjust a single parameter. Parametric studies revealed that the only modification that could match the predicted inner diameter evolution to the LVDT measurements was through the high temperature cohesion parameter, $d_{H.T.}$. Recall that the high temperature properties were estimated from dry, un-bonded sand, which has no cohesion. During casting, the room temperature cohesion ($d_{R.T.}$) of bonded sand thermally degraded with increasing temperatures. However, binder pyrolysis is a kinetic process and the bonded sands can be expected to yield before pyrolysis has completed. Therefore, some amount of cohesion should be expected during yielding. Through a parametric study, the measured and predicted

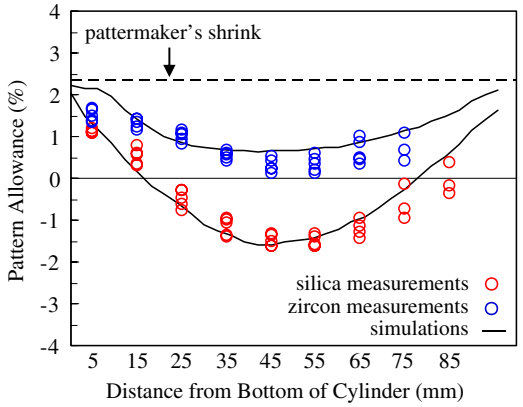


**Figure 14.** Comparison between measured and predicted pattern allowances for the silica and zircon core experiments after adjusting the high temperature cohesion.

**Table 1.** Mechanical properties and Drucker–Prager Cap parameters for the silica bonded sands.

| Temperature (°C) | $E$ (MPa) | $v$ (–) | $\beta$ (°) | $d$ (MPa) | $R$ (–) | $\alpha$ (–) |
|---|---|---|---|---|---|---|
| 20 | 3403 | 0.3 | 55 | 1.85 | 0.45 | 0.01 |
| 180 | 60 | 0.3 | 55 | 0.11 | 0.45 | 0.01 |
| 1600 | 60 | 0.3 | 55 | 0.11 | 0.45 | 0.01 |

**Table 2.** Mechanical properties and Drucker–Prager Cap parameters for the zircon bonded sands.

| Temperature (°C) | $E$ (MPa) | $v$ (–) | $\beta$ (°) | $d$ (MPa) | $R$ (–) | $\alpha$ (–) |
|---|---|---|---|---|---|---|
| 20 | 3403 | 0.3 | 52 | 1.85 | 0.45 | 0.01 |
| 180 | 60 | 0.3 | 52 | 0.08 | 0.45 | 0.01 |
| 1600 | 60 | 0.3 | 52 | 0.08 | 0.45 | 0.01 |

inner diameter expansions for the silica experiments were matched for $d_{H.T.}$ = 0.11 (see Figure 12(a)). Using the same procedure, $d_{H.T.}$ was adjusted from 0 to 0.08 to for the zircon experiments.

Until now, it has been suggested that minimal yielding occurred in the bonded sands at lower temperatures (i.e. before binder pyrolysis). To show this, a parametric study on the critical temperature ($T_{crit}$) for the cohesion parameter was performed. Recall that the critical temperature defines the transition from bonded to un-bonded sand due to binder pyrolysis. Any changes to the critical temperature will alter the low temperature properties. Figure 12(c) illustrates how variations in the critical temperature between 50 and 400 °C affect the cohesion parameter. The sensitivity of the predicted inner diameter evolution to these differences is shown in Figure 12(d). The variations in the predicted change in inner diameter are relatively small (<0.3 mm) when the transition temperature is below 300 °C. This result supports the intuition that the low temperature properties play a small role for the prediction of pattern allowances.

Using the adjusted cohesion values for the silica and zircon bonded sands, the inner diameter evolutions were predicted within the measurement scatter at all times, as shown in Figure 13. Recall that all changes in the inner diameter after solidification were caused by thermal strains (see Figure 6). Thus, the adjustment to the cohesion parameter only affected the predicted inner diameter evolution before solidification. In addition, the simulations predicted the pattern allowances accurately (see Figure 14). Only the zircon pattern allowances at the 5 mm location were not predicted within the scatter of the measurements. This disagreement can be attributed to uncertainties in the predicted temperatures shortly after filling. The final datasets used in the simulations are summarized in Tables 1 and 2 for the silica and zircon sands, respectively.

Figure 15 shows contours of temperatures (a), von Mises stress (b), pressure (c), and equivalent plastic strains (d) at 50 s, 200 s, and 40,000 s (i.e. room temperature). The barrel-shaped profile can be seen after 50 s and is fully-evolved after 200 s. At 50 s, von

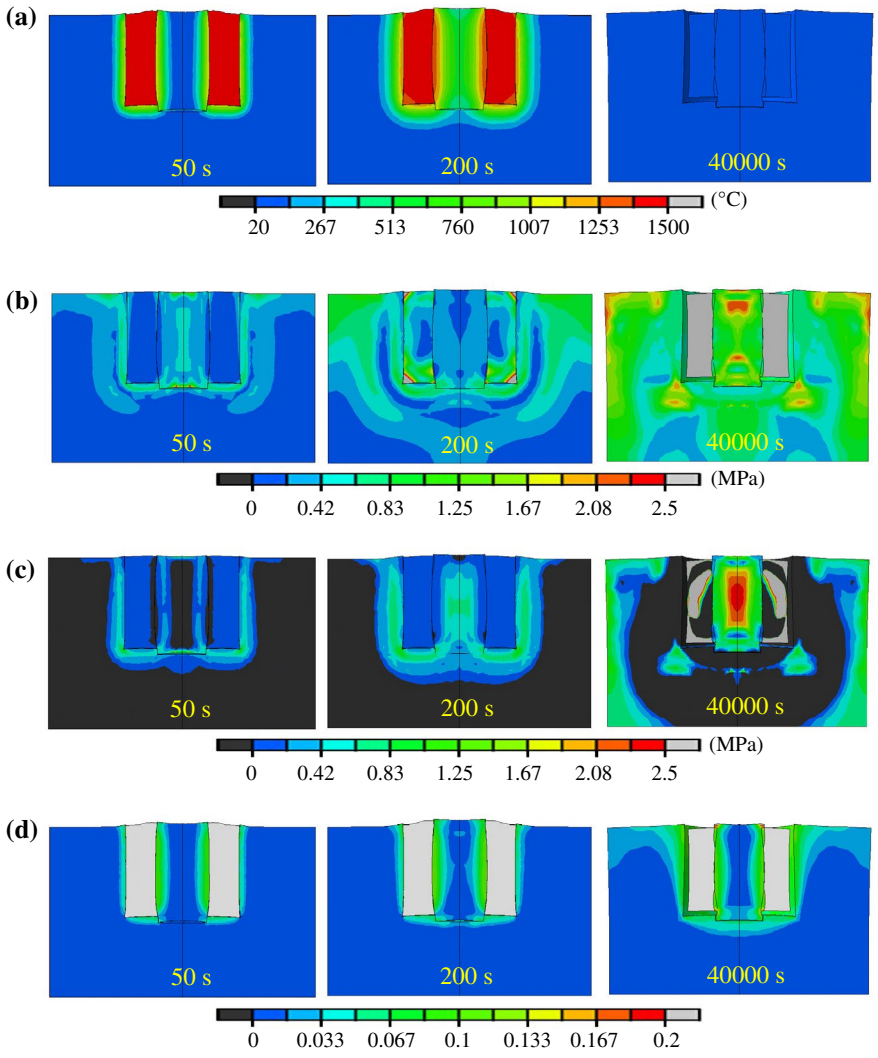


**Figure 15.** Contours of temperature (a), von Mises stress (b), pressure (c), and equivalent plastic strains (d) at 50 s, 200 s, and 40,000 s (room temperature) for the silica core experiments. Distortions magnified by a factor of 5.

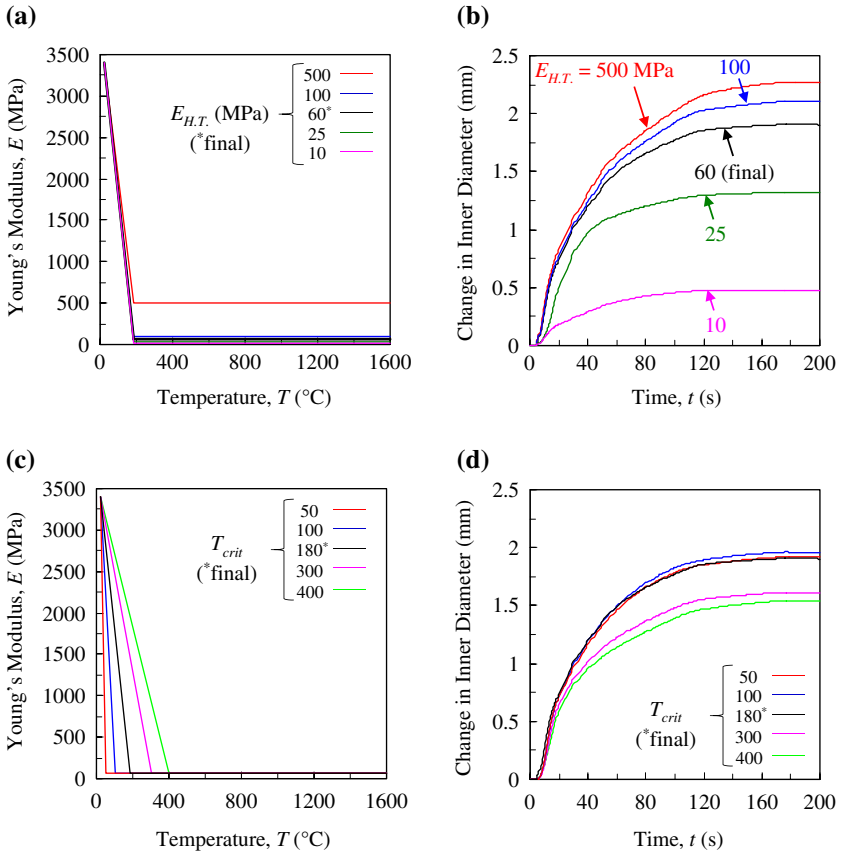


**Figure 16.** Parametric study on Young's modulus demonstrating the effect of changes to $E_{H.T.}$ (a) and $T_{crit}$ (c) on the predicted change in inner diameter (shown in (b) and (d)) for the silica core experiments.

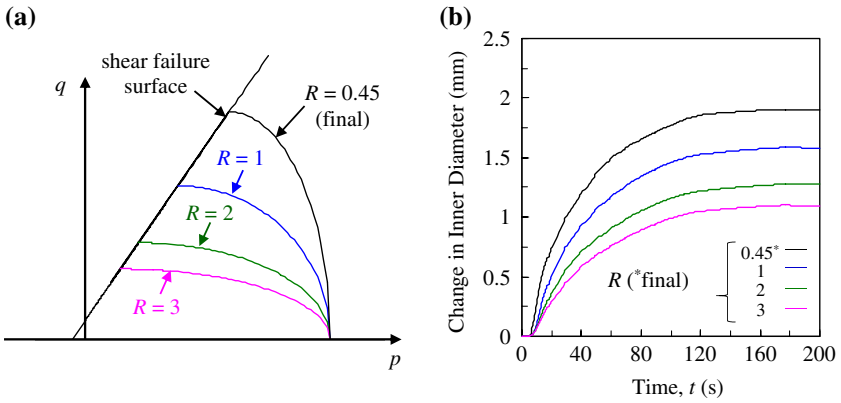


**Figure 17.** Parametric study demonstrating the effect of the cap eccentricity ($R$) on the predicted change in inner diameter for the silica core experiments (a) cap eccentricity (b) change in inner diameter.

Mises stresses, which are a necessary condition for the prediction of dilation, can be seen in excess of 0.25 MPa throughout the core. The combination of these shear stresses with low pressures give rise to significant equivalent plastic strains in the core after 50 s (see Figure 15(d)). A strong correlation between the equivalent plastic strain and temperature contours can also be seen at 50 s, as significant plastic strains are only predicted in the high temperature regions of the mold. This comparison illustrates the minimal yielding that was predicted in the bonded sands at low temperatures.

### 6.3. Parametric studies

The lack of high temperature mechanical measurements raises questions concerning the accuracy of the bonded sand properties used in this study. Certainly, some amount of temperature dependence in the properties can be expected. However, the impact of this dependency on the predicted stresses and strains is unclear. Therefore, this section investigates the uncertainties that are associated with the high temperature bonded sand properties through a series of parametric studies on the silica core experiments (similar results can be expected for the zircon core experiments). These studies will shed

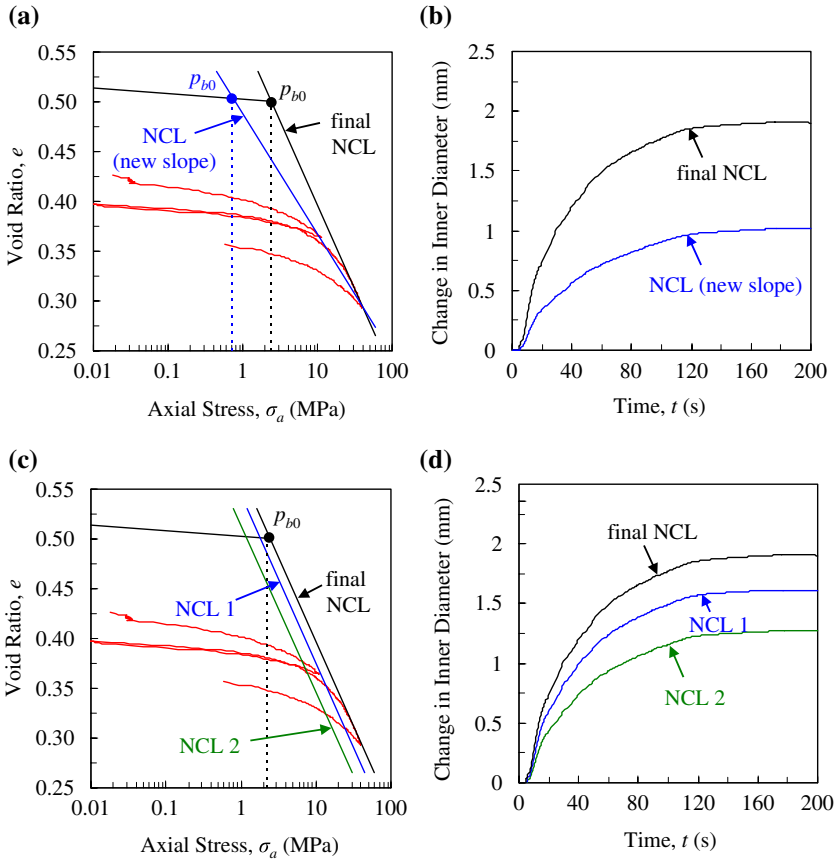


**Figure 18.** Parametric studies demonstrated how changing the slope (a) of and shifting (c) the NCL affects the predicted change in the inner diameter (shown in (b) and (d)) for the silica core experiments.

light on which high temperature parameters are most important and provide a basis for future testing needs.

Figure 16 illustrates the sensitivity of the predicted inner diameter evolution to changes in Young's modulus. In Figure 16(a), $E_{H.T.}$ is varied from 10 to 500 MPa. Using these curves, the predicted inner diameter evolutions in Figure 16(b) become increasingly sensitive as $E_{H.T.}$ decreases. For example, the predicted expansion at 200 s decreases by approximately 0.2 mm (9% reduction) when decreasing $E_{H.T.}$ from 500 to 100 MPa. However, decreasing $E_{H.T.}$ from 25 to 10 MPa has a tremendous impact on the predictions, as the predicted expansion at 200 s decreases from 1.3 to 0.5 mm (62% reduction). Therefore, setting $E$ as a constant above $T_{crit}$ is reasonable as long as its high temperature value is above 100 MPa. Otherwise, a temperature dependency should be considered above the critical temperature.

In addition to $E_{H.T.}$, the critical temperature for Young's modulus was also varied, as shown in Figure 16(c). From the simulation results in Figure 16(d), it is obvious that the inner diameter evolution is only sensitive to changes in the critical temperature for $T_{crit} > 180$ °C. The parametric study on $T_{crit}$ for the cohesion parameter (see Figure 12(c) and (d)) produced similar conclusions. Therefore, based on the parametric studies on $T_{crit,}$ it can be stated with confidence that minimal core expansion due to dilation occurred for temperatures less than 180 °C.

Figure 17 shows that the predicted inner diameter evolution is also sensitive to variations in the cap eccentricity, $R$, which was varied from 0.45 to 3. This result is somewhat counter-intuitive because yielding on the cap surface is associated with compaction, which was not important for the cylinder experiments. The sensitivity of the predicted change in the inner diameter to $R$ can be understood from Figure 17(a). An increase in $R$

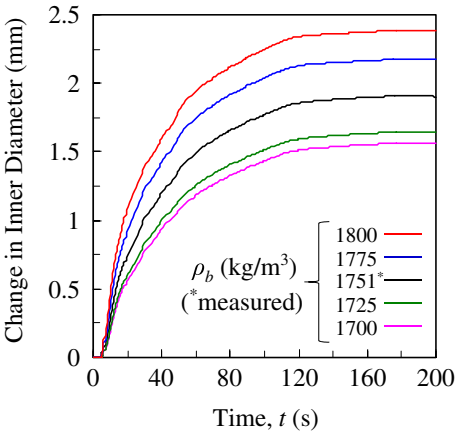


**Figure 19.** Parametric study demonstrating the effect of the initial bulk density on the predicted change in the inner diameter for the silica core experiments.

reduces the span of the shear failure surface, which in turn decreases the amount of predicted dilation. As a result, increasing the value of $R$ decreases the maximum predicted core expansion.

The effect of changes in the NCL were also investigated. The NCL was determined from the slope of 1-D compression test curves at high pressures. Depending on the interpretation of these curves, it could be argued that a different slope should be used, e.g. the 'NCL (new slope)' curve in Figure 18(a). The result of this adjustment is drastic, as the maximum predicted inner diameter expansion (see Figure 18(b)) is roughly half of that from the simulation using the estimated value.

At high temperatures, the hydrostatic compressive strength, $p_b$, of the bonded sand can be expected to decrease somewhat. This reduction can be modeled by shifting the NCL to the left at high temperatures as shown in Figure 18(c). The 'NCL 1' curve reduces the high temperature hydrostatic compressive strength to 75% of the room temperature value, whereas the 'NCL 2' reduces the high temperature value by 50%. As expected, these reductions reduce the maximum predicted inner diameter expansion as shown in Figure 18(d).

The final parametric study is concerned with controlling process conditions rather than studying high temperature properties. For this study, the effect of the initial bulk density on the finite element predictions was investigated. The initial bulk density was varied between 1700 and 1800 kg/m$^3$. Such variations in the density cause significant variations in the predicted change in inner diameter (see Figure 19). These differences illustrate the importance of controlling the packing density during mold construction.

## 7. Conclusions

In this study, the effect of mold expansion on pattern allowances was investigated. Sand casting experiments were performed, in which the inner diameter of a hollow steel cylinder was distorted by core expansion. It was found from the finite element stress simulations that thermal expansion of the bonded sand only generated a small fraction of the observed inner diameter expansion. This prompted the author's to consider sand dilation as the mechanism responsible for the remaining expansion. To predict dilative behavior, the bonded sand used to build the core and mold was modeled using the Drucker–Prager Cap constitutive law. Adjustments to model parameters were needed to predict the correct amount of dilation. By doing so, the barrel-shaped profile of the inner diameter was accurately predicted, as the simulated pattern allowances fell within the scatter of the measurements.

Parametric studies investigated uncertainties associated with the high temperature mechanical properties. The finite element predictions were found to be sensitive to changes in high temperature Young's modulus ($E_{H.T.}$) values less than 60 MPa but relatively insensitive for $E_{H.T.}$ values > 100 MPa. Changes to the cap eccentricity and NCL also impacted the predictions significantly. A final parametric study demonstrated the importance of controlling the packing density when building the molds.

The present study has provided invaluable insight to the physics associated with sand mold expansion during solidification. The findings have not only identified the importance of dilation but have also quantified it. By calibrating the Drucker–Prager Cap model parameters to account for dilation, this represents the first study geared towards predicting casting distortions that are created by sand dilation. Due to the apparent impact of sand dilation on pattern allowances, it is envisioned that the present stress model can have an immediate positive impact on process efficiency for the foundry industry. With the aid of simulation, it is anticipated that the high costs and long lead times associated with pattern design can be drastically reduced. Although the current results are highly encouraging, the parametric studies revealed that further work is needed to better characterize the high temperature properties and mitigate the uncertainties associated with them.

## Acknowledgements

This research was sponsored through the Defense Logistics Agency through the American Metal Consortium and the Steel Founders' Society of America.

## Disclosure statement

No potential conflict of interest was reported by the authors.

## Funding

This research is sponsored by the DLA – Troop Support, Philadelphia, PA and the Defense Logistics Agency Logistics Operations, J335, Research & Development, Ft. Belvoir, VA, under subcontract number 2012-525 from the Advanced Technology Institute, Summerville, SC.

## References

[1] Parkins RN, Cowan A. Effects of mould resistance on internal stress in sand castings. Proceedings of the Institute of British Foundation, paper No. 1953;1062:A101–9.
[2] Mkumbo CSE, Nyichomba BB, Campbell J, et al. Linear contraction of grey iron sand castings. Int J Cast Metals Res. 2002;14:225–234.
[3] Nyichomba BB, Cheya IM, Campbell J. Linear contraction of ductile iron castings. Int J Cast Metals Res. 1998;11:179–186.
[4] Nyichomba BB, Campbell J. Linear contraction and residual stress of aluminium alloy sand castings. Int J Cast Metals Res. 1998;11:163–177.
[5] Motoyama Y, Takahashi H, Inoue Y, et al. Development of a device for dynamical measurement of the load on casting and the contraction of the casting in a sand mold during cooling. J Mater Process Technol. 2012;212:1399–1405.

[6] Monroe C, Beckermann C. Simulation of Hot Tearing and Distortion During Casting of Steel: Comparison with Experiments. 61st Steel Founders Society of America Technical and Operating Conference, paper No. 5.7. Chicago (IL): Steel Founders' Society of America; 2006.
[7] Peters F, Voigt R, Ou SZ, et al. Effect of mould expansion on pattern allowances in sand casting of steel. Int J Cast Metals Res. 2007;20:275–287.
[8] Yamamoto O, Yamada H, Saito M. Properties of furan and oil-urethane nobake binder at room and elevated temperatures. Jpn Foundry. 1978;50:14–18.
[9] Caylak I, Mahnken R. Thermomechanical characterisation of cold box sand including optical measurements. Int J Cast Metals Res. 2010;23:176–184.
[10] Thole J, Beckermann C. Measurement of elastic modulus of PUNB bonded sand as a function of temperature. Int J Metalcast. 2010;4:7–18.
[11] Ami Saada RA, Bonnet G, Bouvard D. Thermomechanical behavior of casting sands: experiments and elastoplastic modeling. Int J Plast. 1996;12:273–294.
[12] Galles D, Beckermann C. In situ measurement and prediction of stresses and strains during casting of steel. Metall Mater Trans A. 2016;47:811–829.
[13] Galles D, Beckermann C. Effect of sand dilation on core expansion during steel casting. IOP Conference Series: Materials Science and Engineering. Vol. 84. Hyogo; 2015.
[14] MAGMA GmbH, MAGMAsoft, Kackerstrasse 11, 52072 Aachen. Germany.
[15] Miettinen J. Calculation of solidification-related thermophysical properties for steels. Metall Mater Trans B. 1997;28:281–297.
[16] Galles D, Beckermann C. Prediction of distortions and pattern allowances during sand casting of a steel bracket. Int J Cast Metals Res. 2016. doi:10.1080/13640461.2016.1262984.
[17] Carlson KD, Beckermann C. Determination of solid fraction-temperature relation and latent heat using full scale casting experiments: application to corrosion resistant steels and nickel based alloys. Int J Cast Metals Res. 2012;25:75–92.
[18] Carniglia SC, Barna CL. Handbook of industrial refractories technology: principles, types, properties and applications. Park Ridge (NJ): Noyes Publications; 1992.
[19] Monroe C. A modeling and experimental study of deformation and hot tearing in steel. [PhD thesis]. Iowa City (IA): University of Iowa; 2009.
[20] Pokorny M, Monroe C, Beckermann C. Prediction of hot tear formation in a magnesium alloy permanent mold casting. Int J Metalcast. 2008;2:41–53.
[21] ABAQUS®. Providence (RI): Abaqus,.
[22] Gens A, Potts DM. Critical state models in computational geomechanics. Eng Comput. 1988;5:178–197.
[23] Saxena SK, Reddy RK, Sengupta A. Verification of a constitutive model for granular materials. Proceedings of the International Workshop on Constitutive Equations for Granular Non-cohesive Soils; Cleveland (OH); 1989. p. 629–645.
[24] Hettler A, Vardoulakis I. Behaviour of dry sand tested in a large triaxial apparatus. Géotechnique. 1984;34:183–197.